

RESEARCH ARTICLE

# Radiation Dose Estimates for [<sup>18</sup>F]5-Fluorouracil Derived from PET-Based and Tissue-Based Methods in Rats

Adam L. Kesner,<sup>1</sup> Wei-Ann Hsueh,<sup>1</sup> Johannes Czernin,<sup>1</sup> Henry Padgett,<sup>2</sup>  
Michael E. Phelps,<sup>1</sup> Daniel H. S. Silverman<sup>1,3</sup>

<sup>1</sup>Molecular and Medical Pharmacology, Ahmanson Biological Imaging Division, UCLA Medical Center, Los Angeles, CA, USA

<sup>2</sup>Siemens Molecular Imaging, Culver City, CA, USA

<sup>3</sup>Nuclear Medicine Clinic, CHS AR-144, UCLA Medical Center, MC694215, Los Angeles, CA 90095-6942, USA

## Abstract

**Introduction:** Radiation dosimetry assessment often begins with measuring pharmaceutical biodistribution in rodents. The traditional approach to dosimetry in rodents involves a radioassay *ex vivo* of harvested organs at different time points following administration of the radiopharmaceutical. The emergence of small-animal positron emission tomography (PET) presents the opportunity for an alternative method for making radiodosimetry estimates previously employed only in humans and large animals. In the current manuscript, normal-tissue absorbed dose estimates for the <sup>18</sup>F-labeled chemotherapy agent [<sup>18</sup>F]5-fluorouracil ([<sup>18</sup>F]5-FU) were derived by PET imaging- and by tissue harvesting-based methods in rats.

**Methods:** Small-animal PET data were acquired dynamically for up to 2 h after injection of [<sup>18</sup>F]5-FU in anesthetized rats (*n*=16). Combined polynomial and exponential functions were used to model the harvesting-based and imaging-based time–activity data. The measured time–activity data were extrapolated to modeled (i.e., Standard Man) human organs and human absorbed doses calculated.

**Results:** Organ activities derived by imaging-based and by harvesting-based methods were highly correlated (*r*>0.999) as were the projected human dosimetry estimates across organs (*r*=0.998) obtained with each method. The tissues calculated to receive highest radiation dose by both methods were related to routes of excretion (bladder wall, liver, and intestines). The harvesting-based and imaging-based methods yielded effective dose (ED) of 2.94E–2 and 2.97E–2 mSv/MBq, respectively.

**Conclusions:** Small-animal PET presents an opportunity for providing radiation dose estimates with statistical and logistical advantages over traditional tissue harvesting-based methods.

**Key words:** Small-animal PET, Radiodosimetry, Interspecies extrapolation, [<sup>18</sup>F]5-fluorouracil

## Introduction

A prerequisite to the use of diagnostic radiotracers in humans is the measurement of organ radiation doses in animals, used to estimate administered activities which will maintain organ doses within an “acceptable” range, while yield-

ing diagnostically useful scintigraphic images. With the introduction of new radiotracers to study the pharmacokinetics and pharmacodynamics of antitumor agents and biological processes *in vivo* with positron emission tomography (PET), there is a need for efficient evaluation of the time-dependent biodistribution of such tracers in animals.

Radiation dose estimates in small animals such as rodents are traditionally derived by sacrificing the animals at various times points after tracer administration, harvesting, and weigh-

ing their organs, and measuring their respective activities [1–3]. As a recent example, the radiation dosimetry of [ $^{18}\text{F}$ ]fluorocholine was calculated on the basis of data from 29 mice killed at 10, 30, 60, or 120 min post-administration, followed by assay of activities in heart, brain, lung, liver, kidneys, and muscle [4]. Larger animals such as monkeys are also often studied with noninvasive imaging methods [5, 6]. Once sufficient data have been obtained to reasonably establish that a given administered activity will yield organ doses within an “acceptable” range, dose estimates can be refined using imaging data from a small number of human subjects [4, 7, 8].

One of the earlier studies which utilized small-animal PET for radiodosimetry measurements was presented by Ugur et al. [9], who showed that the PET imaging agent  $^{66}\text{Ga}$ -DOTA-TOC can be used both diagnostically and to provide quantitative data to be used for radiodosimetry of a tumor and other organs in mice. For this study, the dosimetry was calculated by assuming complete local absorption of non-penetrating radiation, thus allowing for the direct conversion of image-derived activity concentration to radiation dosimetry (using a conversion factor). A limitation of this approach is the simplification that the dosimetry arising from penetrating radiation is nonsignificant. Thus, this methodology does not extend well to assessing other imaging agents/isotopes, which are often selected because of their high penetrating/non-penetrating radiation properties.

In additional radiodosimetry work by Palm et al. [10],  $^{86}\text{Y}$ -Trastuzumab PET was used to measure pharmacokinetic parameters with which to estimate  $^{90}\text{Y}$ -trastuzumab radiodosimetry in mice, for tumor, liver, kidneys, and spleen. This work accounted for some cross-organ absorbed dose (organs mentioned above) using methods based upon the MIRD formalism [11] and murine model-specific geometry/S-factors.

The study presented here investigates the feasibility and accuracy of estimating human radiodosimetry, based upon imaging parameters derived from small-animal-dedicated PET, using [ $^{18}\text{F}$ ]5-FU. As described in more detail in the “Discussion” section, our present study extends and integrates previous work in several ways: In our investigation, we use a robust description of organ biodistribution (source organs in dosimetry calculations) and whole body activity; we are using a fluorine-based compound in small-animal PET; and we are making and testing human dosimetry estimates from extrapolation of biodistribution data across species (from rats to humans) to calculate dosimetry in human-specific geometry.

Fluorouracil was reported to have tumor inhibitory properties by Heidelberger et al. in 1957 [12] and has been established over the subsequent decades to have efficacy against several types of cancers (e.g., colorectal, breast, stomach). Shani and Wolf later pioneered the testing of [ $^{18}\text{F}$ ]-labeled 5-FU to predict tumor response to 5-FU [13].

The radiolabeled form of the fluorouracil compound, [ $^{18}\text{F}$ ]5-fluorouracil ([ $^{18}\text{F}$ ]5-FU), has been studied with PET and examined with respect to its prognostic value for treatment efficacy [14–16]. Based on those early promising studies, [ $^{18}\text{F}$ ]5-FU may be investigated more widely in humans, and

accurate human radiodosimetry for this tracer will be valuable for selecting doses that provide for both high quality images and patient safety with respect to radiation exposure.

## Materials and Methods

All studies were performed under a protocol approved by the UCLA IRB. Sixteen Sprague–Dawley rats (avg. weight: 250 g) were injected with a 1,000- $\mu\text{l}$  solution containing  $\sim 100$  MBq (range: 60–172 MBq) of [ $^{18}\text{F}$ ]5-FU in saline, which was administered via tail vein injection. Rats were anesthetized by inhalation of 2% isoflurane, and images were reconstructed from dynamic acquisitions, with the rat in the prone position, and the long axis of the animal set parallel to the plane of detectors. The acquisitions were executed using a Siemens/CTI Focus 220 small-animal PET scanner (CTI Concorde Microsystems LLC, Knoxville, TN, USA). The 3D list-mode data was sorted using Fourier rebinning. Images were reconstructed using a filtered back projection algorithm with a ramp filter—cutoff equal to the Nyquist frequency, i.e.,  $1.0/(2.0 \times \text{sampling})$ . Data were reconstructed with a pixel size of 0.4 mm and a plane thickness of 0.8 mm in a  $128 \times 128 \times 95$  matrix. Dynamic scans consisted of 10-min time frames, including upper body and lower body bed positions, and all data were decay-corrected to the beginning of the time frame. Image-based organ uptake measurements were derived from organ regions of interest defined on the scan by a single observer. ROIs were defined by drawing spheres in representative organ data spaces relative to visual anatomic landmarks and corresponding atlas images. The bladder ROI was drawn using a threshold region-growing algorithm for a late time frame (volume large enough to encompass all counts in the bladder). Following scans, rats were killed, by intracardiac administration of Nembutal (at 30, 60, 90, and 120 min).

Following scanning, the rat organs were harvested and weighed, and total organ activity content was quantified using a gamma well counter. All the organ activity measurements were normalized to injected activity. In calculating the organ activity content from the image data, the small-animal PET scan measurements were calibrated by comparing the mean organ activity concentration observed in the last frame of the PET image, with the time-corrected harvested organ activity concentration, for each organ, for each rat in order to intrinsically adjust for attenuation, partial volume effects, and counting efficiency. The liver calibration factor was used for organs for which harvesting full activities is difficult (bladder, intestines). Image-based organ activity measurements were made by manually defining regions of interest (ROI) for each organ, calculating the mean activity concentration within the organ ROI, and then calculating total organ activity content by multiplying those concentrations by total harvested organ weight. The bladder volumes were calculated from the scan, and the lung volumes were found by dividing the harvested lung weight by density of 0.296 g/cc [17]. All other organ total volumes were derived from their harvested weights, assuming those tissue densities to be equal to 1 g/cc. All organ activities were assumed to be uniform within each organ. A remainder disintegration value was derived from all the unaccounted-for activity (the difference between the total disintegrations and the organ localized disintegrations).

For comparison purposes, an additional set of image-based biodistribution measurements were also made using a single global calibration factor. Calibration of the small-animal PET scanner was derived using a vial containing a known quantity of  $^{18}\text{F}$  assayed in a dose calibrator (Biodex Atomlab™ 300 Dose Calibrator). Vial

images were reconstructed using the same parameters used in the animal studies, and a global calibration factor was found from comparing the raw PET counts to the known activity concentration. Attenuation correction factors were estimated on an organ by organ basis. The estimations were derived by inflating the Moby digital mouse phantom [18] to the approximate volume of the rats we used. The emission and attenuation data were forward projected, corrected for attenuation, and then backprojected into image space (projections done in 2D). Organ attenuation factors were derived from comparing pre- and post-correction activity values.

A flow chart summarizing the main steps in our methods can be seen in Fig. 1. The three main steps in our methods for calculating dosimetry were as follows. We began by calculating the total number of disintegrations emitted from each particular animal organ. Tracer biodistribution was then extrapolated from rat to human based on relative organ masses. Finally, human dosimetry estimates were generated using dedicated software [19].

Animals were killed at several time points after injection (30, 60, 90, and 120 min). Image-based time–activity curves were generated for the rats that were killed at 120 min, immediately following the final frame of the 120-min acquisitions, and normalized by the activity injected. Time–activity curves were made in a similar manner for the harvested organ activity measurements.

For both harvesting- and imaging-based methods, a second-degree polynomial function ( $f=ax^2+bx+c$ ) was fitted (using Microsoft Excel curve fitting algorithms) to represent the time–activity curve between the time of injection and 120 min later. The time–activity curve for the heart was modeled using two polynomial functions, one representing initial blood pool uptake (0–15 min), and the other representing the rest of the scan data. At 120 min after injection, biological distribution was considered stable, and physical decay of the isotope was modeled as a monoexponential function. By integrating the modeled activity curves from injection time out to infinity, we calculated the disintegrations attributed to each organ

from a unit of injected activity (1 MBq), accounting for both biological half-life as well as physical half-life.

This process was repeated for all organs for both the imaging and harvested data. All measurements were also corrected for a mean measured 2% of total activity remaining in the tail. For bladder measurements, we used a non-voiding bladder model. These estimates can thus be regarded as conservative for those patients who are capable of significant urine excretion.

For the harvested organ-based dosimetry set, the bladder and intestinal percent activity data used were derived from the imaging-based calculations, since some of the radioactive content of urine and feces would otherwise be lost and unaccounted for during the organ-harvesting process.

Several methods have been previously described for extrapolating organ uptake data in animals to equivalent uptake in humans [7]. For this study, we used the proposed method of Kirschner et al. [20] based upon a percent kilogram dose per gram (% kg dose/g) unit:

$$\begin{aligned} (\% \text{ kg dose/g}) &= \frac{\left(\frac{\%}{\text{organ}}\right)_{\text{animal}}}{g_{\text{organ,animal}}} * \text{kg}_{\text{animal}} \\ &= \frac{\left(\frac{\%}{\text{organ}}\right)_{\text{human}}}{g_{\text{organ,human}}} * \text{kg}_{\text{human}} \end{aligned}$$

Assuming this parameter is constant across species, one can calculate equivalent organ activities across different organisms, after establishing weight of each organ in each of the species (we used the mean weight of the organs harvested from the animals and standard weights established for the adult male human organs [17]).

Using the imaging- and the harvesting-based organ time–activity data in rats, the respective human-equivalent organ time–activity data were thus derived and cumulated activities calculated. The total body residence time was calculated to be 2.64 h (100% ×

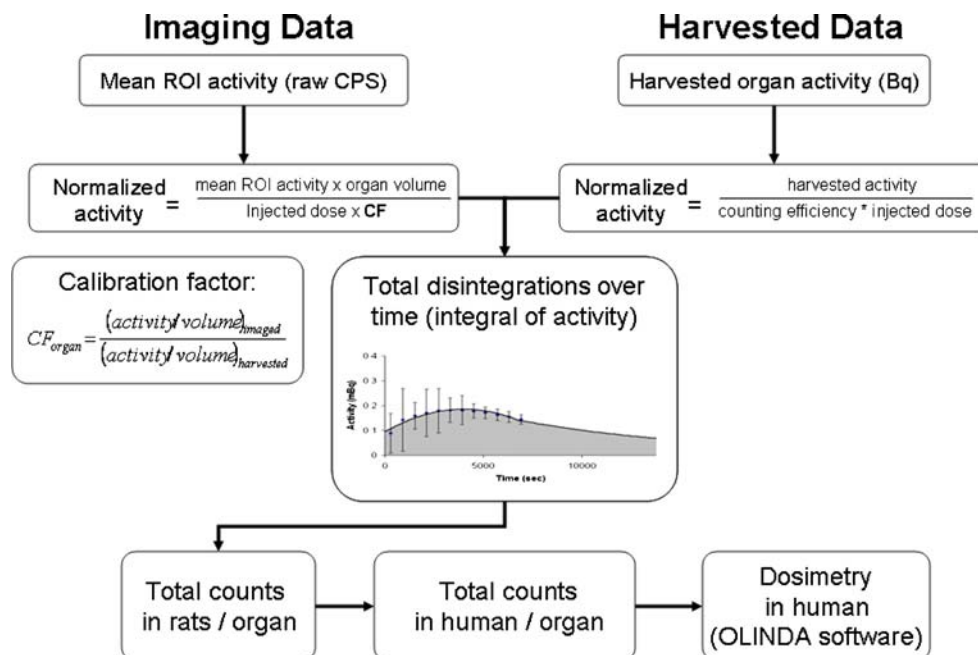


Fig. 1. Flow chart illustrating methods used to project human  $^{18}\text{F}$ 5-FU dosimetry, derived from harvesting- and imaging-based rodent measurements.

1/ $\lambda$ ). With those data, we applied OLINDA/EXM [19] MIRD-based [21] human dose estimation software to obtain human organ dose estimates.

The SD of the dose delivered to individual organs was calculated using the following equation, similar to previously used methods [22–24]:

$$\sigma_{Di}^2 = \sum_j S_{ij}^2 * \sigma_j^2$$

Where  $\sigma_{Di}$  is the standard deviation (SD) of the estimated dose for the  $i$ th organ,  $S_{ij}$  is the  $S$  value for the dose to the  $i$ th target organ from the  $j$ th source organ (mGy/MBq-s), and  $\sigma_j$  is the SD of the integrated activity for the  $j$ th source organ.

The source organ SD ( $\sigma_j$  in the above equation) was designed to account for the interindividual variation of the image-based time course measurements relative to the gold-standard measurements derived from the harvested data. To find its magnitude for each respective organ, polynomial and exponential models were fit to time–activity curves representing mean organ measurements  $\pm 1$  SD, with the SD derived from the spread of the activity measurements derived at each particular time point. An example of the  $\pm$ SD window can be seen for the liver in Fig. 2. These  $\pm$ SD ranges were then normalized by the 120-min calibration time point, and extrapolated to the human biodistribution data set, thus generating an associated  $\sigma_j$  to use in the above dosimetry error equation.

## Results

Time–activity data in rats were acquired both by dynamic PET imaging and by radioassay of harvested organs (Table 1). Percent total disintegrations emitted from each organ calculated with imaging- and harvesting-based data are shown in Table 2. The Pearson correlation coefficient between these data sets was  $>0.999$ , with or without inclusion of the excretory-related organs (bladder and intestines) in the correlation assessment.

Human activity distribution projected from our rat-based measurements is displayed in Fig. 3, and resultant human

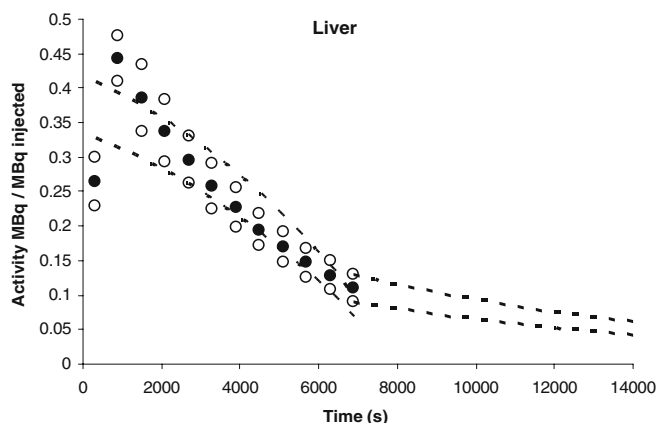


Fig. 2. Illustration of error window (mean $\pm$ SD) used to calculate source organ SD for the liver. The *solid black points* represent the mean activity–time curve data, and the *hollow points* represent the bounds at a distance of  $\pm 1$  SD.

radiodosimetry estimates are displayed in Table 3. This figure and table also display the values corresponding to the activity distribution based entirely on rat image data (i.e., scanner-based calibration rather than harvested organ-based calibration).

Harvesting- and imaging-based dosimetry measurements both illustrated that the organs receiving highest radiation dose were the bladder wall, liver, and intestines, but image-based data demonstrated less interindividual variation than harvest-based data (e.g., see liver time–activity curves in Fig. 4). When used to calculate dosimetry for  $^{18}\text{F}$ 5-FU in humans, both the harvest- and image-based methods would give comparable estimates of a safe dose, in terms of both effective dose (2.94E–2 vs to 2.97E–2 mSv/MBq, respectively), as well as of dose to critical organs. The relative contributions to organ dose from beta and gamma emissions were 47% and 53%, respectively, for the harvested-based distribution and were 48% and 52% for the imaging-based distribution.

## Discussion

Using imaging (i.e., PET)-based methods, we have determined that for an administered activity of 750 MBq of  $^{18}\text{F}$ 5-FU to Standard Man, the doses to critical organs including the bladder wall, liver, small intestines, and lower large intestines would be 93, 65, 54, and 54 mSv, respectively—well within the range considered acceptable for diagnostic Nuclear Medicine procedures [7, 25]. We can also compare our radiodosimetry estimates with published dosimetry estimates from a more widely used fluorinated pyrimidine:  $^{18}\text{F}$  fluorothymidine (FLT) [22], Effective dose equivalent measurements (as described in ICRP 53) for FLT and our imaging based  $^{18}\text{F}$ 5-FU were 2.8E10–2, and 3.26E10–2 mSv/MBq, respectively. Both the FLT dosimetry set and our  $^{18}\text{F}$ 5-FU dose estimates identified the urinary bladder wall, the liver, and the kidneys as being organs receiving high levels of radiation dose (1.79E–01, 4.51E–02, 3.52E–2 mGy/MBq for FLT, and 1.24E–01, 8.69E–02, 3.74E–02 mGy/MBq for 5-FU, respectively).

Determining tissue distribution of 5-FU [26, 27], and of its  $^{18}\text{F}$ -labeled analog [28, 29], has been of long-standing interest. Harvesting-based dosimetry for  $^{18}\text{F}$ 5-FU was first published in 1982 by Shani et al. [30]. They studied a group of 12 rats injected with a dose of  $^{18}\text{F}$ 5-FU and killed at 30-60- and 120-minute time points following injection. For dosimetry calculations in that article, the uptake was considered instantaneous, having a measured effective half-life within the organs. Tracer biodistribution was considered similar enough to humans to allow for a reasonable estimation. Residence times were calculated for 11 major organs from the rat measurements, and residence times for the bladder were based on urine-based data actually collected from one human patient. They projected that the organ receiving the highest radiation dose in humans would be the bladder wall, as was also the case for our study



**Table 1.** Activity distribution measurements (rat)

Organ	Mean ( $n=4$ ) harvesting-based organ activity (MBq), $t=120$ min ( $\pm$ SD)	Harvesting-based organ cumulative activity (MBq s) (area under fitted curve)	Imaging-based organ activity (MBq), $t=120$ min ( $\pm$ SD)	Imaging-based organ cumulative activity (MBq-s) (area under fitted curve)
Heart	5.85E+02 $\pm$ 1.62E+02	1.22E+01	5.80E+02 $\pm$ 1.47E+02	2.09E+01
Liver	1.11E+05 $\pm$ 2.14E+04	2.68E+03	1.10E+05 $\pm$ 1.97E+04	2.82E+03
Thyroid	4.32E+02 $\pm$ 1.60E+02	8.70E+00	4.51E+02 $\pm$ 2.49E+02	1.49E+01
Bladder	7.17E+02 $\pm$ 2.26E+02	1.18E+01	1.43E+05 $\pm$ 4.75E+04	2.49E+03
Colon	2.62E+03 $\pm$ 6.06E+02	6.02E+01	8.26E+04 $\pm$ 2.00E+04	2.01E+03
Lungs	1.01E+03 $\pm$ 2.97E+02	2.13E+01	3.03E+02 $\pm$ 1.03E+02	6.33E+00
Spleen	5.90E+02 $\pm$ 1.20E+02	1.21E+01	5.95E+02 $\pm$ 1.58E+02	2.18E+01
Kidneys	9.59E+03 $\pm$ 3.72E+03	2.11E+02	9.45E+03 $\pm$ 3.49E+03	3.13E+02
SmInt	6.73E+03 $\pm$ 1.57E+03	3.08E+02	8.42E+04 $\pm$ 3.46E+04	1.63E+03
Brain	2.35E+02 $\pm$ 8.30E+01	5.27E+00	2.37E+02 $\pm$ 1.06E+02	4.12E+00
Stomach	9.52E+03 $\pm$ 8.98E+03	1.33E+02	8.22E+03 $\pm$ 6.84E+03	1.38E+02

Measurements for the [<sup>18</sup>F]5-FU tracer radio-distribution of activity in rats

(Table 3). If we compare our imaging-based bladder wall radiation dose estimate of 0.124 mGy/MBq to the bladder wall [<sup>18</sup>F]5-FU dose estimate by Shani et al. of 0.197 mGy/MBq, it is seen that the dosimetry of the bladder wall projected from imaging rat bladders (as we have done), has a value close to that based upon a study of direct measurements of urine from humans.

Qualitative data supporting interspecies extrapolation performed here comes from a human [<sup>18</sup>F]5-FU PET scan acquired clinically at our facility. Figure 5 shows a side by side comparison of rat and human [<sup>18</sup>F]5-FU PET scans. Visual inspection of the figure illustrates the similarities in the biodistribution of the radiotracer in both species, with activity in both cases predominantly concentrated in tissues reflecting routes of excretion. As another way of providing external validation of the dosimetry estimates obtained here,

we also compared them to the results of work that had been performed in monkeys (from IND application: no. 57,954, provided courtesy of Peter Conti). This study projected the whole body effective dose equivalent (for standard man) to be 2.70E<sup>-2</sup> mSv/MBq (extrapolated from monkeys), which was similar to our image-based EDE estimate of 3.26E<sup>-2</sup> mSv/MBq (extrapolated from rats).

In the present work, we have taken an approach to estimate [<sup>18</sup>F]5-FU human dosimetry, with methodology that builds upon prior investigations. Previous work utilizing small-animal PET-based determinations of biodistribution of <sup>66</sup>Ga-DOTA-TOC [9] relied upon the assumption that the radioactive content of each organ served as the sole source of the radiation exposure for that organ. Fuller modeling of the relationship between PET images and radiopharmaceutical dosimetry followed in work with <sup>86</sup>Y-trastuzumab, which utilized PET-based activity concentration measurement for murine dosimetry derived from MIRD-based calculations [10]. We have

**Table 2.** Percent injected dose (PID) estimated for humans

Organ	PID		Organ weight (kg)
	Harvesting (%)	Imaging (%)	
Liver	24.3	25.6	0.316
SmInt + cnt*	11.4	11.4	1.910
Bladder + Cnt*	9.1	9.1	0.021
Lwr Colon + cnt*	3.7	3.7	0.259
Kidneys	1.1	1.7	0.310
Lungs	0.6	0.6	1.000
Stomach + cnt	0.5	0.6	0.183
Brain	0.2	0.1	0.299
Heart wall	0.1	0.2	1.100
Spleen	0.1	0.2	1.420
Thyroid	0.0	0.0	0.413
Remainder	48.7	46.7	66.47
Body			73.70
Pearson correlation coefficient			0.99995
Pearson correlation coefficient without* organs			0.99979

Radiotracer distributions resulting from measurements based on imaging, and harvesting projected to human biodistributions (units in percent injected dose per kilogram, cnt Contents)

\* denotes harvested measurements taken from image based calculations

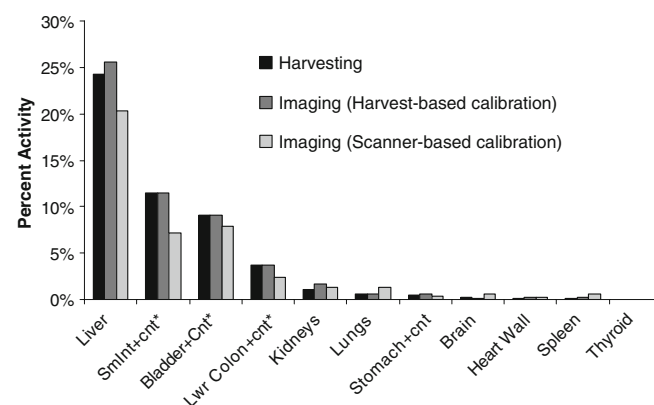


**Fig. 3.** Percent total organ disintegration measurements (cumulative activity) of [<sup>18</sup>F]5-FU calculated in humans based upon small-animal imaging-based and harvesting-based activity data. (\*) denotes harvested measurements taken from image based calculations.

**Table 3.** Radiation dosimetry estimates

Dosimetry (mSv/MBq)					
Organ	Harvesting	Imaging (scanner-based calibration)	Imaging (harvest-based calibration)		
			SD	Beta/photon ratio	
Urinary bladder					
Wall	1.24E-01	1.09E-01	1.24E-01	1.18E-02	1.97
Liver	8.27E-02	6.99E-02	8.69E-02	6.65E-03	1.32
LLI wall	7.24E-02	5.14E-02	7.22E-02	7.32E-03	2.19
Small intestine	7.20E-02	5.00E-02	7.18E-02	2.43E-02	2.63
Kidneys	2.84E-02	3.03E-02	3.74E-02	7.59E-03	1.23
Gallbladder					
Wall	2.44E-02	2.22E-02	2.50E-02	2.29E-03	0.10
ULI wall	2.25E-02	1.90E-02	2.25E-02	4.27E-03	0.12
Uterus	2.24E-02	2.02E-02	2.22E-02	3.60E-03	0.12
Ovaries	2.11E-02	1.84E-02	2.09E-02	3.76E-03	0.13
Stomach wall	1.66E-02	1.57E-02	1.68E-02	2.34E-03	0.59
Adrenals	1.51E-02	1.53E-02	1.56E-02	2.49E-03	0.18
Pancreas	1.51E-02	1.54E-02	1.55E-02	2.63E-03	0.18
Total body	1.22E-02	1.22E-02	1.22E-02	2.19E-03	0.56
Osteogenic					
Cells	1.20E-02	1.33E-02	1.17E-02	–	0.75
Red marrow	1.01E-02	1.02E-02	1.00E-02	2.28E-03	0.20
Spleen	1.01E-02	2.21E-02	1.33E-02	3.97E-03	0.58
Heart wall	9.94E-03	1.18E-02	1.15E-02	2.42E-03	0.33
Muscle	9.56E-03	1.00E-02	9.43E-03	2.10E-03	0.33
Lungs	9.25E-03	1.28E-02	9.38E-03	2.17E-03	0.31
Testes	9.20E-03	9.80E-03	8.95E-03	2.08E-03	0.35
Thymus	7.66E-03	8.83E-03	7.52E-03	2.18E-03	0.45
Breasts	6.73E-03	7.56E-03	6.63E-03	1.78E-03	0.55
Skin	6.38E-03	7.03E-03	6.24E-03	–	0.60
Thyroid	6.14E-03	7.99E-03	7.54E-03	2.29E-03	0.77
Brain	2.27E-03	4.41E-03	2.04E-03	1.89E-03	0.22
Effective dose (mSv/MBq)	2.94E-02	2.54E-02	2.97E-02		
Correlation with Harvesting		0.9850	0.9977		

Estimated radio-dosimetry resulting from measurements based upon rat imaging and organ harvesting (OLINDA output)

approached radio-dosimetry derived from small-animal PET, with the aim to develop a standardized methodology for this application. Our work involved the use of rats, rather than mice, which by comparison in size, allows for greater accuracy in activity measurements. Secondly, we made an effort to more fully account for the distribution of all the injected activity throughout the rats. That included measuring activity concen-

tration for 11 organs, as well as making certain that the total activity in the organs and the whole body remainder accounted for 100% of the expected activity. We followed up upon using

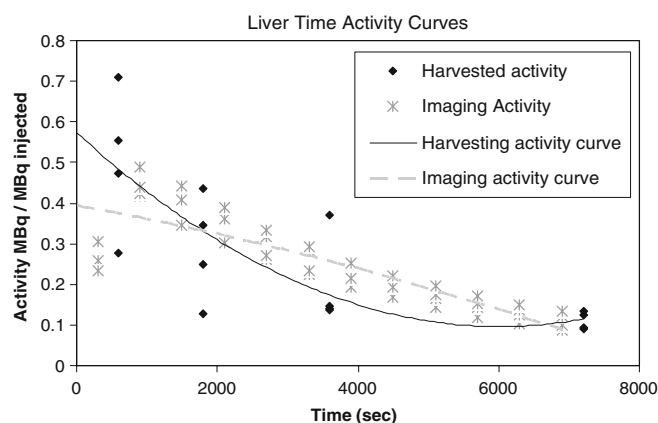


**Fig. 4.** Time–activity curves for the liver, for harvesting- and imaging-based methods.

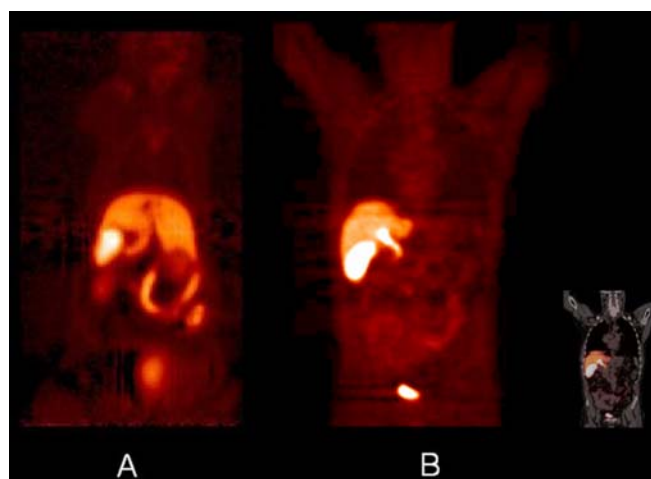


**Fig. 5.** Small animal (a) and human (b) PET images acquired after administration of  $^{18}\text{F}$ 5-FU (rat image acquired on Siemens/CTI Focus 220 small-animal PET scanner and human image acquired on a Siemens/CTI Biograph PET/CT scanner). Rat image is a summed image (60 min, two bed positions) acquired following 0.68 Mbq/g injection.

rodent data for biodistribution measurements as an appropriate early step for projecting human biodistribution, with human radiodosimetry estimates that were more accurately projected by using a human anatomical model. Our methods include subject-specific biodistribution extrapolations from the measured sources to a model phantom from which the dosimetry was derived, with corresponding S-factors [17]. Finally, we applied these methods to the [ $^{18}\text{F}$ ]-labeled chemotherapy agent, [ $^{18}\text{F}$ ]-5-FU, and presented updated radiodosimetry data for this tracer, comparing or externally validating those data in multiple ways (to harvested rat organ measurements, qualitative comparison to whole-body human distribution, and quantitative comparison to human dosimetry projected from large-animal studies).

There are, in principle, several advantages to utilizing PET data of small animals for radiation dosimetry purposes. First, only a fraction of the animals currently used for that purpose need to be purchased and maintained, and far fewer animals need to be killed. Further along those lines, the number of hours involved in dissecting and processing tissues, homogenizing or dissolving them in organic solvents, and doing scintillant-based or direct gamma counting decreased, and the overall time from the start of a dosimetry-determination project to its conclusion can be abbreviated. Third, the time course of radiotracer distribution in an individual animal, which is intended to model what would occur in an individual human subject receiving the dose actually measured, rather than having to be inferred from assembling cross-population data as is traditionally done. This not only requires fewer animals because of the multiple time points of data that can be obtained per animal, but also increases the statistical stability of the data because each individual is serving as its own across-time control, avoiding time point by point variance caused by interindividual differences.

Harvesting radioactivity in organs represents a direct method of quantifying activity distribution. While it is not prone to scatter, attenuation, or other sources of image degradation which can affect imaging data, the method does have some disadvantages. Generating time-activity curves from harvested organs adds to the burden of number of overall animals needed, and the labor required to generate dosimetry data. Additionally, measurements based upon harvesting certain organs like the heart, bladder, or intestines, which are often important contributors to dosimetric analysis, are problematic due to loss of blood, urine, or feces occurring during the harvesting process, respectively. Imaging-based measurements, in contrast, are relatively quick and easy to make, requiring fewer specimens and person-hours. With imaging, regional volumes can also be measured without invasive procedures.

The largest difference in overall expense, work, and time in the methods we have presented follows from the fewer rats needed to be studied using the imaging-based methods, as well as substituting organ ROIs in image analysis software for sacrificing animals, dissecting the animals to recover individual organs at each time point, weighing the organs, and assaying

the radioactivity levels in the extracted tissue. The first process took about 15 min for each animal at one time point after tracer administration, while the latter process required approximately three times as long. Moreover, once the organ ROIs were defined for a particular animal at one time point, they could be used for the measurements made at the other sampled time points (e.g., at 10-min intervals), while for the harvested data, the whole measurement process needs to be repeated for each sampled time point. Once all the data are acquired, the data analysis work is comparable using either method.

With the dose of [ $^{18}\text{F}$ ]-5-FU used in this study (approximately 0.5 MBq/g), we were able to observe well-defined contours on organs that had taken up moderate levels of activity. This dose was comparable to amounts used to study radiolabeled chemotherapy agents in rodents in previously published work [31–33].

[ $^{18}\text{F}$ ]-5-FU like many tracers studied have a majority of tracer concentration, beyond the perfusion stage, located predominantly in organs involved as routes of excretion (e.g., liver, genitourinary structures). It would be valuable to confirm generalizability of this approach for those tracers that do have a large percentage of uptake in other organs.

Projecting pharmaceutical biodistribution and radiotracer dosimetry across species from small animals to humans can be useful for accelerating the development of radioactive compounds to be used in clinical settings, and is a common first step, consistent with the recommendations of ICRP 62 [7], prior to moving forward with human measurements from a small number of volunteers. This strategy is grounded upon an initial estimate that “partition of activity among various tissues, organs, and excretory routes is broadly similar in investigational animals and man” [4]. Along those lines, we have provided a comparison to human radiodosimetry estimates derived here and those derived from prior work with a primate model and found them to be substantially similar.

To the extent that small-animal imaging-based methods can be used in place of harvesting-based methods, that process may be facilitated by the kind of approach illustrated here.

## Conclusions

Small-animal PET imaging-based dosimetry compares well with dosimetry estimates generated by more traditional methods (i.e., measurements derived from harvested organs), appears less prone to the data scatter associated with interindividual variation which is inherent in cross-population harvested-based methods, and can be carried out utilizing less time and labor, as well as fewer animals. As this approach is validated with other tracers with substantially different types of distributions, it may prove useful for simply and rapidly obtaining radiodosimetry estimates, as a step in the process of allowing new tracers to be developed for use in humans.

*Acknowledgement.* This work is supported by National Institutes of Health/ National Cancer Institute, through an ICMIC program grant (project director DHSS).

## References

- Tang G, Wang M, Tang X, Luo L, Gan M (2003) Pharmacokinetics and radiation dosimetry estimation of *O*-(2-[ $^{18}\text{F}$ ]fluoroethyl)-L-tyrosine as oncologic PET tracer. *Appl Radiat Isot* 58:219–225
- DeGrado TR, Baldwin SW, Wang S, Orr MD, Liao RP, Friedman HS et al (2001) Synthesis and evaluation of ( $^{18}\text{F}$ )-labeled choline analogs as oncologic PET tracers. *J Nucl Med* 42:1805–1814
- Santens P, De Vos F, Thierens H, Decoo D, Slegers G, Dierckx RA et al (1998) Biodistribution and dosimetry of carbon-11-methoxyprogabidic acid, a possible ligand for GABA-receptors in the brain. *J Nucl Med* 39:307–310
- DeGrado TR, Reiman RE, Price DT, Wang S, Coleman RE (2002) Pharmacokinetics and radiation dosimetry of  $^{18}\text{F}$ -fluorocholine. *J Nucl Med* 43:92–96
- Deterding TA, Votaw JR, Wang CK, Eshima D, Eshima L, Keil R et al (2001) Biodistribution and radiation dosimetry of the dopamine transporter ligand. *J Nucl Med* 42:376–381
- Kurziel KA, Kiesewetter DO, Carson RE, Eckelman WC, Herscovitch P (2003) Biodistribution, radiation dose estimates, and *in vivo* Pgp modulation studies of  $^{18}\text{F}$ -paclitaxel in nonhuman primates. *J Nucl Med* 44:1330–1339
- ICRP Publication 62: Radiological Protection in Biomedical Research. *Annals of the ICRP Volume 22/3: International Commission on Radiological Protection*; 1993
- Schmidt D, Langen KJ, Herzog H, Wirths J, Holschbach M, Kiwit JC et al (1997) Whole-body kinetics and dosimetry of L-3-123I-iodo-alpha-methyltyrosine. *Eur J Nucl Med* 24:1162–1166
- Ugur O, Kothari PJ, Finn RD, Zanzonico P, Ruan S, Guenther I et al (2002) Ga-66 labeled somatostatin analogue DOTA-DPhe1-Tyr3-octreotide as a potential agent for positron emission tomography imaging and receptor mediated internal radiotherapy of somatostatin receptor positive tumors. *Nucl Med Biol* 29:147–157
- Palm S, Ennon RM Jr, Matei C, Kolbert KS, Xu S, Zanzonico PB et al (2003) Pharmacokinetics and Biodistribution of ( $^{86}\text{Y}$ )-Trastuzumab for ( $^{90}\text{Y}$ ) dosimetry in an ovarian carcinoma model: correlative MicroPET and MRI. *J Nucl Med* 44:1148–1155
- Loevinger R, Budinger T, Watson E (1988) *MIRD primer for absorbed dose calculations*. Society of Nuclear Medicine, New York, NY
- Heidelberger C, Chaudhuri NK, Danneberg P, Mooren D, Griesbach L, Duschinsky R et al (1957) Fluorinated pyrimidines, a new class of tumour-inhibitory compounds. *Nature* 179:663–666
- Shani J, Wolf W (1977) A model for prediction of chemotherapy response to 5-fluorouracil based on the differential distribution of 5-[ $^{18}\text{F}$ ]fluorouracil in sensitive versus resistant lymphocytic leukemia in mice. *Cancer Res* 37:2306–2308
- Bellemann ME, Brix G, Haberkorn U, Ostertag HJ, Lorenz WJ (1994) Drug-specific  $^{19}\text{F}$  NMR and dynamic  $^{18}\text{F}$  PET imaging of the cytostatic agent 5-fluorouracil. *IEEE Trans Nucl Sci* 41:2856–2861
- Bading JR, Alauddin MM, Fissekis JD, Shahinian AH, Joung J, Spector T et al (2000) Blocking catabolism with eniluracil enhances PET studies of 5-[ $^{18}\text{F}$ ]fluorouracil pharmacokinetics. *J Nucl Med* 41:1714–1724
- Dimitrakopoulou-Strauss A, Strauss LG, Schlag P, Hohenberger P, Mohler M, Oberdorfer F et al (1998) Fluorine-18-fluorouracil to predict therapy response in liver metastases from colorectal carcinoma. *J Nucl Med* 39:1197–1202
- Cristy M, Eckerman K (1987) Specific absorbed fractions of energy at various ages from internal photon sources. Oak Ridge National Laboratory, Oak Ridge, TN
- Segars WP, Tsui BM, Frey EC, Johnson GA, Berr SS (2004) Development of a 4-D digital mouse phantom for molecular imaging research. *Mol Imaging Biol* 6:149–159
- Stabin MG, Sparks RB, Crowe E (2005) OLINDA/EXM: the second-generation personal computer software for internal dose assessment in nuclear medicine. *J Nucl Med* 46:1023–1027
- Kirschner A, Ice R, Beierwaltes W (1975) Letters to the editor. *J Nucl Med* 16:248–249
- Siegel JA, Thomas SR, Stubbs JB, Stabin MG, Hays MT, Koral KF et al (1999) MIRD pamphlet no. 16: techniques for quantitative radiopharmaceutical biodistribution data acquisition and analysis for use in human radiation dose estimates. *J Nucl Med* 40:37S–61S
- Vesselle H, Grierson J, Peterson LM, Muzi M, Mankoff DA, Krohn KA (2003)  $^{18}\text{F}$ -Fluorothymidine radiation dosimetry in human PET imaging studies. *J Nucl Med* 44:1482–1488
- Mankoff DA, Peterson LM, Tewson TJ, Link JM, Galow JR, Graham MM et al (2001) [ $^{18}\text{F}$ ]fluoroestradiol radiation dosimetry in human PET studies. *J Nucl Med* 42:679–684
- Bevington P, Robinson D (1992) *Data Reduction and Error Analysis for the Physical Sciences*, 2nd ed. McGraw-Hill, New York, NY
- ICRP Publication 53: Radiation Dose to Patients from Radiopharmaceuticals. International Commission on Radiological Protection; 1987
- Brix G, Bellemann ME, Gerlach L, Haberkorn U (1998) Intra- and extracellular fluorouracil uptake: assessment with contrast-enhanced metabolic  $^{19}\text{F}$  MR imaging. *Radiology* 209:259–267
- Brix G, Bellemann ME, Haberkorn U, Gerlach L, Bachert P, Lorenz WJ (1995) Mapping the biodistribution and catabolism of 5-fluorouracil in tumor-bearing rats by chemical-shift selective  $^{19}\text{F}$  MR imaging. *Magn Reson Med* 34:302–307
- Kissel J, Brix G, Bellemann ME, Strauss LG, Dimitrakopoulou-Strauss A, Port R et al (1997) Pharmacokinetic analysis of 5-[ $^{18}\text{F}$ ]fluorouracil tissue concentrations measured with positron emission tomography in patients with liver metastases from colorectal adenocarcinoma. *Cancer Res* 57:3415–3423
- Visser GW, Gorree GC, Peters GJ, Herscheid JD (1990) Tissue distribution of [ $^{18}\text{F}$ ]-5-fluorouracil in mice: effects of route of administration, strain, tumour and dose. *Cancer Chemother Pharmacol* 26:205–209
- Shani J, Young D, Schlesinger T, Siemsen JK, Chlebowski RT, Bateman JR et al (1982) Dosimetry and preliminary human studies of  $^{18}\text{F}$ -5-fluorouracil. *Int J Nucl Med Biol* 9:25–35
- Hsueh WA, Kesner AL, Gangloff A, Pegram MD, Beryt M, Czernin J et al (2006) Predicting chemotherapy response to paclitaxel with  $^{18}\text{F}$ -fluoropaclitaxel and PET. *J Nucl Med* 47:1995–1999
- Gangloff A, Hsueh WA, Kesner AL, Kiesewetter DO, Pio BS, Pegram MD et al (2005) Estimation of paclitaxel biodistribution and uptake in human-derived xenografts *in vivo* with ( $^{18}\text{F}$ )-fluoropaclitaxel. *J Nucl Med* 46:1866–1871
- Kesner AL, Hsueh W-A, Htet NL, Pio BS, Czernin J, Pegram MD, Phelps ME, Silverman DHS (2007) Biodistribution and predictive value of  $^{18}\text{F}$ -fluorocyclophosphamide in mice bearing human breast cancer xenografts. *J Nucl Med* 48:2021–2027; First published on November 15, 2007